

Nonlinear Ocean Wave Reconstruction Algorithms Based on Simulated Spatiotemporal Data Acquired by a Flash LIDAR Camera

Frédéric Nougier, Stéphan T. Grilli, and Charles-Antoine Guérin

Abstract—We report on the development of free surface reconstruction algorithms to predict ocean waves, based on spatial observations made with a high-frequency Flash light detection and ranging camera. We assume that the camera is mounted on a vessel, in a forward looking position, and is pointing at some distance ahead of its path yielding a sample of spatiotemporal wave elevation data. Because of the geometry, the density of measurement points gradually decreases (i.e., becomes sparse) with the distance to the camera. Free surface reconstruction algorithms were first developed and validated for linear 1-D and 2-D irregular surface models, whose amplitude coefficients are estimated on the basis of minimizing the mean square error of simulated surface elevations to measurements, over space and time (for a specified time initialization period). In the validation tests reported here, irregular ocean surfaces are generated on the basis of a directional Pierson-Moskowitz or Elfouhaily spectrum, and simulated LIDAR data sets are constructed by performing geometric intersections of laser rays with each generated surface. Once a nowcast of the ocean surface is estimated from the (simulated) LIDAR data, a forecast can be made of expected waves ahead of the vessel, for a time window that depends both on the initialization period and the resolved wavenumbers in the reconstruction. The process can then be repeated for another prediction window, and so forth. To reconstruct severe sea states, however, nonlinear effects must be included in the sea surface representation. This is done, here, by representing the ocean surface using the efficient Lagrangian choppy wave model [1].

Index Terms—Analytical wave models, Flash LIDAR camera, free surface reconstruction algorithms, linear and nonlinear waves, ocean waves.

I. INTRODUCTION

IN MANY ocean engineering applications where ocean wave information is needed, it is often sufficient to use phase-averaged wave data, usually in the form of a directional wave energy spectrum. For some applications, however, both more accurate and detailed phase resolved, real time, wave data are required. This is for instance the case when predicting

seakeeping and anticipating the motions of a surface vessel, based on measurements of the ocean surface made ahead of its trajectory. Here, the free surface must be reconstructed in real time from a limited number of measurements, which requires applying so-called free surface reconstruction algorithms. In the last decade, new techniques were proposed in the microwave domain for the reconstruction of surface elevation maps [2]–[5], using radar systems at grazing incidence angles. Here, we report on the development and application of reconstruction and prediction algorithms for the ocean surface, based on spatiotemporal data acquired at high frequency by a Flash LIDAR camera [(FLC) such as designed by Advanced Scientific Concepts Inc.; Santa Barbara, California, USA]. An FLC generates a $n \times n$ matrix of laser rays (with $n = 64$ – 128 in the currently existing design), providing n^2 simultaneous measurements of the distance from the FLC to the ocean surface. The camera can be mounted on a vessel (on top of a mast), in a forward looking position, pointing at some distance ahead of its path. From the measured data and the camera's location and orientation, as well as known vessel's motions, the elevation and horizontal position of the measured surface points can be generated in an absolute coordinate system.

A shallow angle (vessel mounted) LIDAR scanning system was already proposed by [6] and field tested for wave profiling up to distances of hundreds of meters, for 1-D cases (i.e., in a vertical plane). As indicated by the authors, since laser rays are first reflecting off of the nearest ocean wave crests (through wave shadowing effects), the density of measurement points inevitably gradually decreases with the distance to the camera even if the horizontal sampling is regular. Hence, this results in a highly spatially nonuniform distribution of ocean surface elevation values/data (as, e.g., sketched in Fig. 1), as a function of time (i.e., a spatiotemporal data set), based on which the ocean surface must be reconstructed.

Although a linear reconstruction should be sufficient for the short-term forecast of moderate sea states, to better estimate more severe sea states and predict them later in time, nonlinear effects must be included in the sea surface representation. In addition to changing wave steepness, such effects also influence the wave phase speed that increasingly affects the forecast as time increases. The use of second- and third-order (and even higher-order) free surface models in ocean wave reconstruction algorithms was investigated by [7]–[9]. The proposed nonlinear models, however, were all quite computationally demanding, particularly in a reconstruction mode. Here, we represent nonlinear sea surfaces through the efficient Lagrangian model choppy wave (CW), which was

Manuscript received May 14, 2012; revised March 13, 2013; accepted March 14, 2013. Date of publication May 29, 2013; date of current version December 17, 2013. The work of Stéphan T. Grilli was supported by the U.S. Navy STTR Program, managed by the Office of Naval Research, Code 333, under Contract N0001410M0277.

F. Nougier and C.-A. Guérin are with the Université de Toulon (CNRS/INSU, IRD, MIO, UM 110), La Garde Cedex 83957, France, and also with the Aix-Marseille Université (CNRS/INSU, IRD, MIO, UM 110), Marseille 13288, France (e-mail: frederic.nougier@gmail.com; guerin@univ-tln.fr).

S. T. Grilli is with the Department of Ocean Engineering, University of Rhode Island, Narragansett, RI 02881 USA (e-mail: grilli@oce.uri.edu).

Color versions of one or more of the figures in this paper are available online at <http://ieeexplore.ieee.org>.

Digital Object Identifier 10.1109/TGRS.2013.2254494

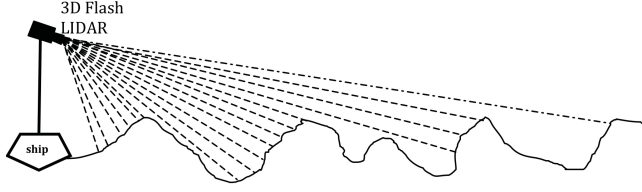


Fig. 1. Sketch of Flash-LIDAR angle of view of the ocean surface and visualization of a few rays (1-D situation). Measurement points are sparse far from the ship.

demonstrated to correctly approximate second-order properties of waves with narrow-banded spectra [1] and to be accurate enough for most sea states, as long as there are limited decimeter gravity waves. The CW model is used in the proposed reconstruction algorithms.

In Sections II and III, we present the development and validation of new free surface reconstruction algorithms based on a linear or second-order representations of 1-D and 2-D irregular ocean surfaces, whose parameters are estimated through minimizing the mean-square error of simulated surface elevations to measurements made over space and time (for a specified time prediction window). If sea state is properly estimated, a prediction of expected waves ahead of the camera/vessel can be made; the process is then repeated for another prediction window, and so forth. Our methods and results apply to fully 2-D ocean surfaces (Section V).

II. OCEAN FREE SURFACE REPRESENTATION

In this paper, we consider ocean surface representations based either on linear superposition [10] or on the nonlinear CW model, which is an extension of Gertsner's wave theory [1]. As a reminder, linear Stokes wave theory shows that for any wave harmonic of wavenumber k_n (wavelength λ_n) and circular frequency ω_n , (period T_n), the dispersion relationship

$$\frac{\omega_n^2}{g} = k_n \tanh k_n h \quad \text{with} \quad \omega_n = \frac{2\pi}{T_n}; \quad k_n = \frac{2\pi}{\lambda_n} \quad (1)$$

and the group velocity

$$c_{gn} = \frac{d\omega_n}{dk_n} = \frac{g}{2\omega_n} \tanh(k_n h) \left\{ 1 + \frac{2k_n h}{\sinh(2k_n h)} \right\} \quad (2)$$

holds at second-order (in water depth h , where g denotes the gravitational acceleration). Amplitude dispersion effects, which are not included in these equations, only appear at third and higher orders. Other characteristics, such as wave crest and trough elevations, wave slopes, however, differ at second order. In deep water, (1) and (2) simplify to $\omega_n^2 = gk_n$ and $c_{gn} = g/(2\omega_n)$.

Hence, the linear superposition of $n = 1, \dots, N$ individual wave harmonics of elevation A_n and direction Θ_n yields the linear ocean surface representation, in the horizontal plane of coordinates $\mathbf{x} = (x, y)$

$$\eta(\mathbf{x}, t) = \sum_{n=1}^N A_n \cos(\Psi_n - \varphi_n); \quad \Psi_n = k_{nx}x + k_{ny}y - \omega_n t \quad (3)$$

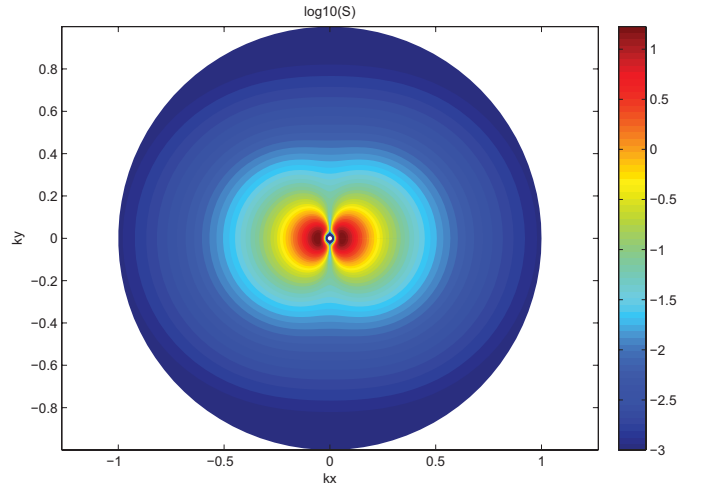


Fig. 2. Directional EY wavenumber spectrum for a significant wave height $H_s = 2.62$ m and spectral peak wavelength $\lambda_p = 88$ m.

where Ψ_n are spatiotemporal phase functions, $\varphi_n = 2\pi \mathcal{R}_n$ are mutually independent (i.e., random) phases, with $\mathcal{R}_n \in [0, 1]$ a set of uniformly distributed random numbers, and $(k_{xn}, k_{yn}) = k_n \{x \cos \Theta_n + y \sin \Theta_n\} = \mathbf{k}_n \cdot \mathbf{x}$, with $\mathbf{k}_n = k_n (\cos \Theta_n, \sin \Theta_n) = k_n \hat{\mathbf{k}}_n$, with $\hat{\mathbf{k}}_n = (\cos \Theta_n, \sin \Theta_n)$, the unit wavenumber vectors (where $\Theta_n \in [0, 2\pi]$ denotes a direction of propagation).

To simplify the following mathematical and algorithm developments, related to free surface reconstruction, it is more convenient (and numerically accurate) to use the equivalent linear representation

$$\eta(\mathbf{x}, t) = \sum_{n=1}^N |k_n|^{-3/2} \{a_n \cos \Psi_n + b_n \sin \Psi_n\} \quad (4)$$

where $\{a_n, b_n; n = 1, \dots, N\}$ are $2N$ wave harmonic parameters describing the ocean surface, with

$$a_n = |k_n|^{3/2} A_n \cos \varphi_n; \quad b_n = |k_n|^{3/2} A_n \sin \varphi_n. \quad (5)$$

The factors $|k_n|^{-3/2}$ constitute a preconditioning, which anticipates the fact that the harmonic amplitude coefficients are related to the square root of the energy density spectrum (see below). This preconditioning will make for better conditioned matrices in the reconstruction algorithms discussed later.

The CW ocean surfaces are obtained from linear surfaces, such as (4), based on the transformation

$$(\mathbf{x}, \eta(\mathbf{x}, t)) \rightarrow (\mathbf{x} + \mathbf{D}(\mathbf{x}, t), \eta(\mathbf{x}, t)) \quad (6)$$

where $\mathbf{D}(\mathbf{x}, t)$ is the spatial Riesz transform (Hilbert transform in 1-D) of η . It can be shown [1] that this transformation introduces a phase quadrature with respect to the original signal; hence, it writes

$$\mathbf{D}(\mathbf{x}, t) = \sum_{n=1}^N |k_n|^{-3/2} \{-a_n \sin \Psi_n + b_n \cos \Psi_n\} \hat{\mathbf{k}}_n. \quad (7)$$

The nonlinear surface, $\tilde{\eta}$ is thus implicitly defined as

$$\tilde{\eta}(\mathbf{x} + \mathbf{D}(\mathbf{x}, t), t) = \eta(\mathbf{x}, t). \quad (8)$$

The horizontal displacement \mathbf{D} is assumed small enough that there are no multiple-valued points in the abscissa transformation and the correspondence between $\tilde{\eta}$ and η is univocal; i.e., in 1-D, there exists an increasing function $\xi = \Phi(x)$ such that $x = \xi + D(\xi)$. This is the case if the condition $|D'| < 1$ is satisfied, which imposes a restriction on the ocean surface slopes, since D and η can easily be shown to have the same rms slope.

In the ocean, we assume that the wave amplitude of each component can be found from a (discretized) directional energy density spectrum $S(\mathbf{k}_n) = S(k_n, \Theta_n)$ (or $S(\omega_n, \Theta_n)$); these two forms being related through (1) as

$$A_n = \sqrt{2S(k_n, \Theta_n) k_n \Delta k \Delta \Theta}. \quad (9)$$

In the following applications, when generating ocean surfaces (whether linear or nonlinear), we will either assume an omnidirectional discrete Pierson–Moskowitz spectrum (PM) for fully developed open seas, or a directional discrete Elfouhaily spectrum (EY). Here, the PM spectrum is defined for both positive and negative wavenumbers as

$$S(k_n) = \frac{\alpha}{2|k_n|^3} \exp\left(-\frac{\beta g^2}{k_n^2 U_{19.5}^4}\right) \quad (10)$$

with the Philips constant $\alpha = 4.05 \cdot 10^{-3}$, $\beta = 0.74$, and $U_{19.5}$ the wind speed at 19.5 m above the surface. For the PM spectrum, the dominant wave angular frequency is defined as, $\omega_p = 0.877g/U_{19.5}$, with in deep water $k_p = \omega_p^2/g$ and hence a dominant wavelength $\lambda_p = 8.17 U_{19.5}^2/g$; (9) also simplifies to $A_n = \sqrt{2S(k_n) \Delta k}$.

The directional Elfouhaily spectrum (EY) [11] is defined by way of an omnidirectional curvature function $B(k_n)$ and a directional spreading function $\delta(k_n)$. The total directional density spectrum writes

$$S(k_n, \Theta_n) = \frac{B(k)}{2\pi k_n^4} (1 + \delta(k_n) \cos(2\Theta_n)) \quad (11)$$

where Θ_n is the direction of wave component n relative to the wind direction. The detailed definitions of $B(k_n)$ and $\delta(k_n)$ can be found in [11]; both are function of wind speed measured at 10 m above the ocean surface U_{10} and wave age Ω (which is related to fetch). The spectral peak wavenumber is defined as

$$k_p = \frac{g\Omega^2}{U_{10}^2} \quad (12)$$

which corresponds to a dominant wavelength $\lambda_p = 8.6 U_{10}^2/g$ for fully developed open seas (i.e., $\Omega = 0.84$).

For PM or EY spectra, the sea state significant wave height is related to the zeroth spectral moment m_0 by

$$H_s = 4\sqrt{m_0} ; m_0 = \sigma^2 = \sum_{n=1}^N S(k_n, \Theta_n) k_n \Delta k \Delta \Theta \quad (13)$$

where σ denotes the standard deviation of the ocean free surface. Combining (1)–(13), one can also generate a EY spectrum for specified (H_s, T_p) values.

In the applications, the target ocean free surfaces will be generated, for PM or EY spectra, using a fast Fourier transform

(FFT). To do so, one first sets low and high frequency, or wavenumber, cutoff values (k_{\min}, k_{\max}) and use N wavenumbers k_n defined on a linear scale in between these values. In practice, k_{\min} is related to the maximum wavelength that can be represented in the sea state, $\lambda_{\max} = 2\pi/k_{\min}$, which is also used as the discretized surface characteristic dimension, and k_{\max} is related to the sampling wavenumber to satisfy Shannon's condition: $k_{\max} = k_e/2$, where k_e is the sampling wavenumber.

Fig. 2 shows an example of a directional EY spectrum, with $U_{10} = 10$ m/s (note $U_{10} \simeq 0.91U_{19.5}$) for a significant wave height $H_s = 2.62$ m, and a peak spectral wavelength $\lambda_p = 88$ m.

III. FREE SURFACE RECONSTRUCTION ALGORITHMS

Assuming a set of observations of the free surface elevation made at M times, using a LIDAR camera with J active rays (i.e., actually intersecting the free surface), i.e., $\eta_{j,m} = \eta(\mathbf{x}_j, t_m)$; $l = j, \dots, J$; $m = 1, \dots, M$, one wishes to reconstruct the ocean surface geometry over some specified range of wavelengths: $(\lambda_{\min}^r, \lambda_{\max}^r)$. In the following, we present reconstruction algorithms based on a linear or first-order (choppy) representation of the free surface. These consist in optimizing the values of $2N$ unknown parameters (a_n, b_n) by minimizing a cost function expressing the rms difference between the reconstructed surface values and the observations.

Owing to the lack of actual data at this time, we validate the proposed algorithms using numerically simulated LIDAR data, extracted from randomly generated ocean surfaces (i.e., linear or choppy), having a specified wave energy spectrum as detailed in the previous section. In the validation applications, both 1-D and 2-D (linear or choppy) cases will be presented and discussed.

A. Linear Ocean Free Surface Reconstruction

Here, we assume that the ocean surface is represented by (4). The simplest minimization of differences between model and observations can be achieved through applying a straightforward least square method. Therefore, we define a cost function for the measured spatiotemporal data points η_l ($l = 1, \dots, L = J \cdot M$) as

$$C = \frac{1}{L} \sum_{l=1}^L (\eta(\mathbf{x}_l, t_l) - \eta_l)^2 \quad (14)$$

where $\eta(\mathbf{x}_l, t_l)$ are the unknown reconstructed surface elevations and η_l are the observations. An extremum of this function is reached for

$$\frac{\partial C}{\partial a_m} = 0, \quad \frac{\partial C}{\partial b_m} = 0 ; m = 1, \dots, N. \quad (15)$$

Developing these equations yields a linear system of $2N$ equations for $2N$ unknown parameters ($m = 1, \dots, N$)

$$\begin{aligned} & \sum_{l=1}^L \sum_{n=1}^N |k_n|^{-3/2} \{a_n \cos \Psi_{ml} \cos \Psi_{nl} + b_n \cos \Psi_{ml} \sin \Psi_{nl}\} \\ & = \sum_{l=1}^L \eta_l \cos \Psi_{ml} \end{aligned}$$

$$\begin{aligned} & \sum_{l=1}^L \sum_{n=1}^N |k_n|^{-3/2} \{a_n \sin \Psi_{ml} \cos \Psi_{nl} + b_n \sin \Psi_{ml} \sin \Psi_{nl}\} \\ &= \sum_{l=1}^L \eta_l \sin \Psi_{ml} \end{aligned} \quad (16)$$

where wave harmonic phases are defined as, $\Psi_{nl} = \mathbf{k}_n \cdot \mathbf{x}_l - \omega_n t_l$. This linear system can be recast in matrix form as

$$A_{mn} X_n = B_n ; X_n = [a_1..a_N, b_1..b_N] \quad (17)$$

where X_n is a vector made of the $2N$ unknown parameters

$$B_n = \left\{ \begin{array}{l} \sum_{l=1}^L \eta_l \cos \Psi_{nl}; \quad 1 \leq n \leq N \\ \sum_{l=1}^L \eta_l \sin \Psi_{nl}; \quad N+1 \leq n \leq 2N \end{array} \right\} \quad (18)$$

and, A_{mn} the $2N \times 2N$ matrix

$$\begin{aligned} A_{mn} &= \sum_{l=1}^L |k_n|^{-3/2} \cos \Psi_{ml} \cos \Psi_{nl} \\ A_{m,N+n} &= \sum_{l=1}^L |k_n|^{-3/2} \cos \Psi_{ml} \sin \Psi_{nl} \\ A_{N+m,n} &= \sum_{l=1}^L |k_n|^{-3/2} \sin \Psi_{ml} \cos \Psi_{nl} \\ A_{N+m,N+n} &= \sum_{l=1}^L |k_n|^{-3/2} \sin \Psi_{ml} \sin \Psi_{nl}. \end{aligned} \quad (19)$$

The linear system (17) is solved at each step of data acquisition (for data acquired at the current and earlier time steps), using either the direct Gauss elimination method or, for larger systems, the more efficient iterative method GMRES. As an example, 7.58 s on a three-year-old basic laptop are needed for a typical inversion with $N_k = 400$ and $L = N_v \times N_h \times N_t = 16,384$, where $N_v = 64$, $N_h = 64$, and $N_t = 4$ is the number of temporal acquisition steps before the inversion is performed.

B. Choppy Ocean Free Surface Reconstruction

Here, we assume that the ocean surface is represented by (8), using the definition of \mathbf{D} in (7). As before, we use a quadratic cost function to optimize the reconstructed surface amplitude parameters (a_n, b_n) with respect to $L = M \cdot J$ spatiotemporal observations η_l , as

$$\tilde{C} = \frac{1}{L} \sum_{l=1}^L (\tilde{\eta}(y_l, t_l) - \eta_l)^2 \quad (20)$$

where y_l is the horizontal coordinate of the set of observations points on the surface. For each y_l , we can find \mathbf{x}_l such that

$$y_l = \mathbf{x}_l + \mathbf{D}(\mathbf{x}_l, t_l). \quad (21)$$

Using this equation in (20) and the implicit definition (8) of the nonlinear surface, we recast the cost function as

$$\tilde{C} = \frac{1}{L} \sum_{l=1}^L (\eta(\mathbf{x}_l, t_l) - \eta_l)^2 \quad (22)$$

where η is the underlying linear surface taken at the horizontal coordinates \mathbf{x}_l .

The extremum condition is thus still defined by (15), which results in the same linear system of equations, however, with the important difference that now η_l and η are elevations taken at different horizontal coordinates. As \mathbf{D} and thus \mathbf{x}_l and all Ψ_{nl} are unknown, we need to proceed iteratively to find them jointly with η . Since in choppy the nonlinear surface is close to the linear one, we begin the iterative process by assuming that $\mathbf{x}_l^{(0)} = y_l$ (i.e., $\mathbf{D} = 0$). Solving the system of equations yields a first solution $(\tilde{a}_n^{(0)}, \tilde{b}_n^{(0)})$, which allows deriving a better estimate of \mathbf{x}_l : $\mathbf{x}_l^{(1)} = y_l - \mathbf{D}^{(0)}(\mathbf{x}_l^{(0)}, t_l)$. This iterative process can thus formally be defined as in equation (23), shown at the bottom of the page, where superscripts in parentheses refer to the iteration number. Step (a) is achieved by solving the system (17) and step (b) via applying the definition in (4) and (7). It should be noted that the first step is equivalent to a linear reconstruction. Practically, convergence is reached after only a few iterations. Hence, a nonlinear inversion usually takes three or four times longer to compute than a linear inversion.

IV. RECONSTRUCTION AND PREDICTION OF 1-D SURFACES

A. Effect of Nonlinearity on Nowcast and Forecast

As a preliminary step, we would like to insist on the need for considering a nonlinear time-evolution to achieve an accurate wave forecast, even though this is much less crucial for nowcast. Therefore, we compare the linear and nonlinear reconstructions of a 1-D ocean surface (with waves traveling only in the positive x direction), independently from the data acquisition method (i.e., LIDAR camera or otherwise) and data type (e.g., dense or sparse). Hence, we simply assume that the data set of observations is constituted of all the points used for numerically generating the ocean surface. A nonlinear ocean surface is generated using choppy (with $N = 2048$ wavenumbers), assuming a PM spectrum with a wind speed $U_{19.5} = 7$ m/s, yielding a dominant wavelength $\lambda_p = 44$ m and wavenumber $k_p = 0.14$ rad/m (10). A linear surface is first generated using the random phase method, by way of a FFT with 2048 points over 200 m (3) and (9), and then transformed into a nonlinear surface through the choppy transformation (6).

Both linear and nonlinear free surface reconstructions are performed with $N_k = 400$ wavenumbers k_n , and two or three iterations are needed for a nonlinear reconstruction. The observation data set used in the reconstruction is the whole surface sampling (i.e., with 2048 points). The expected footprint area of a typical forward-looking LIDAR camera is assumed to be around 100-m wide, and a unique snapshot of the surface will not be sufficient for the accurate reconstruction of a larger wave. The reconstructed surface spectrum will thus be necessarily truncated. We consequently fixed the reconstructed wavenumber vector to be logarithmically spaced in between $k_{\min} = 2\pi/\lambda_{\max}$ and $k_{\max} = 2\pi/\lambda_{\min}$, with $\lambda_{\max} = 200$ m and $\lambda_{\min} = 2$ m, with λ_{\max} thus being more or less the longest wave that can be inverted.

$$\mathbf{x}_l^{(n+1)} = y_l - \mathbf{D}^{(n)}(\mathbf{x}_l^{(n)}, t_l) \quad \xrightarrow{(a)} \quad (\tilde{a}_n^{(n+1)}, \tilde{b}_n^{(n+1)}) \quad \xrightarrow{(b)} \quad (\eta^{(n+1)}, \mathbf{D}^{(n+1)}) \quad (23)$$

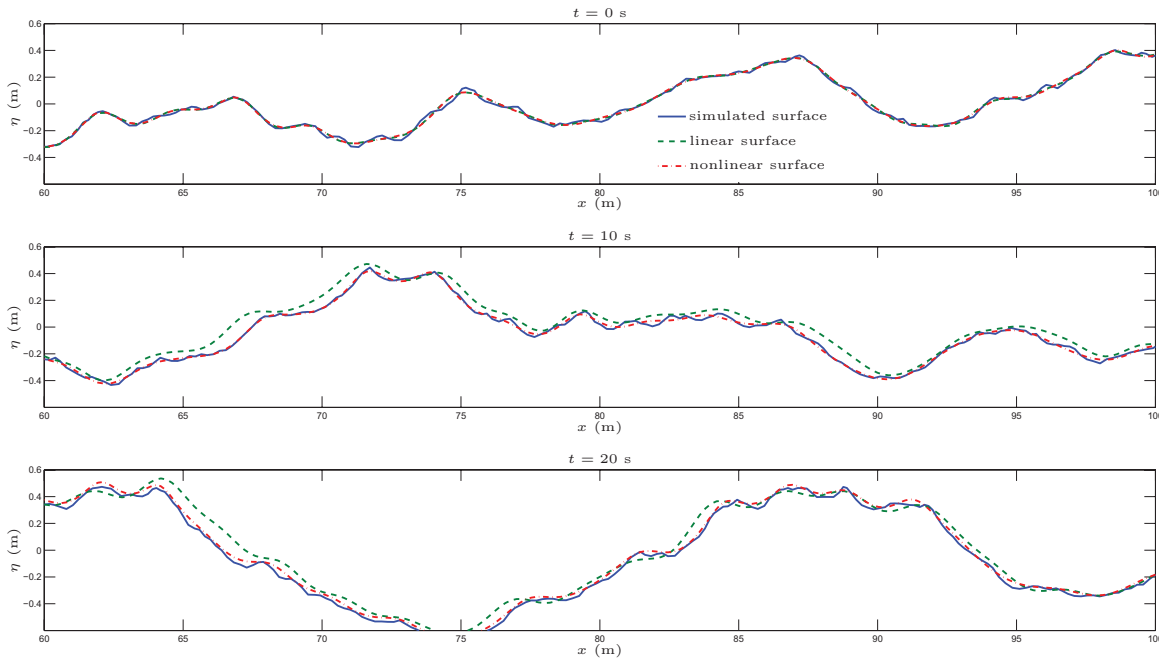


Fig. 3. Linear and nonlinear reconstructions of a time evolving 1-D choppy wave surfaces, at $t=0$, $t=10$, and $t=20$ s. A PM spectrum is assumed with a wind speed $U_{19.5} = 7$ m/s.

Fig. 3 shows a sample of the simulated, and the linear and nonlinear reconstructed, surfaces at different times, for a PM spectrum and a wind speed $U_{19.5} = 7$ m/s. Surfaces at time > 0 are obtained by time updating the phase functions Ψ s. For the nowcast ($t = 0$), errors between reconstructed and simulated surfaces are small and mainly because of the poor reconstruction of shorter waves (because of the reduced number of higher harmonics in the reconstruction). The linear and nonlinear reconstructions are equally accurate, because our reconstruction methodology relies on a cost function minimization. For the forecast at $t = 10$ and 20 s, there is an increasing discrepancy with time between the reconstructed and simulated surfaces, and more so for the linear reconstruction (at $t = 10$ s, the nonlinear reconstruction is very accurate, except for some shorter waves). This is shown in Fig. 4, which shows the ratio $\epsilon/\tilde{\epsilon}$ of linear to nonlinear relative errors in the reconstruction as a function of the forecasting time, and for four different wind speeds (over $x \in [0, 100]$ m and averaged for 50 surfaces both for statistical purposes and to provide smoother curves). As expected, the ratio increases with time and wind speed (thus wave height) because the nonlinearity increases and affects the whole spectrum for larger waves. Hence, using a nonlinear reconstruction method becomes increasingly necessary, the stronger the wind and the steeper the waves. For wind speed as small as 10 m/s, the reconstruction error can be divided by a factor of 8 when using the nonlinear method.

As waves propagate in a nonlinear manner for the simulated choppy surfaces (i.e., they are subjected to amplitude dispersion effects), the estimated coefficients of the linear reconstruction (a_n, b_n) will change at each time step. Therefore, forecasting the time evolution of the reference surface based on such linear coefficients leads to gradually increasing errors with time. By contrast, coefficients estimated with the nonlinear scheme (\tilde{a}_n, \tilde{b}_n) remain nearly identical at each time

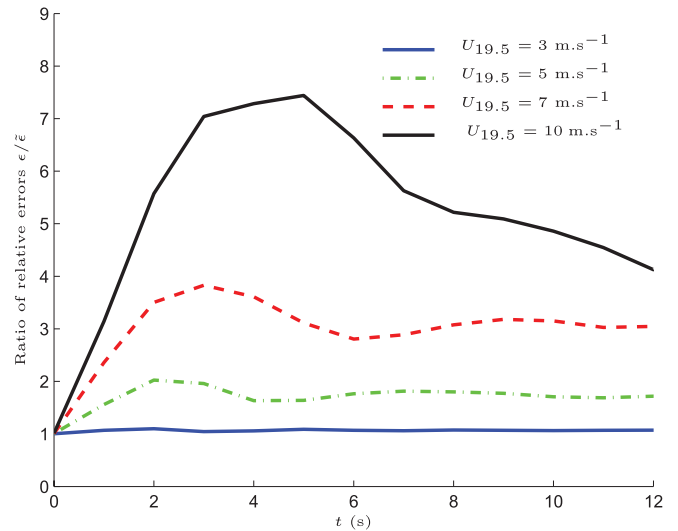


Fig. 4. Ratio of relative errors of the linear to nonlinear reconstructions as a function of the forecasting time.

step and, hence, discrepancies between the nonlinear forecasts and simulated surfaces remain small, as compared with the linear forecast.

Finally, since $(\tilde{a}_n, \tilde{b}_n)$ are only slowly varying in time, as compared with (a_n, b_n) including observations made at different times, the cost function minimization will improve the nonlinear reconstruction. By contrast, using different observation times in the linear reconstruction of a nonlinear surface does not really help and could even be detrimental to the forecast when nonlinearities appear.

B. Generation and Reconstruction Using 1-D LIDAR Data

Here, we consider one of the sea states used earlier, described by a PM spectrum with $U_{19.5} = 10$ m/s, and create

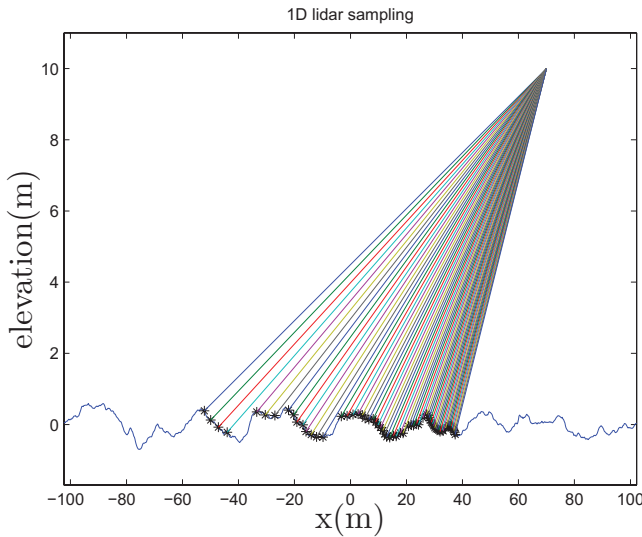


Fig. 5. Example of 1-D LIDAR camera sampling of a nonlinear surface.

a simulated LIDAR data set by calculating the geometric intersections of a series of LIDAR rays with 1-D simulated free surfaces, as a function of space and time (e.g., Fig. 5). The spectrum has been cut-off in the lower and higher wavenumber ranges such that $k_{\min} = 2\pi/w$ and $k_{\max} = 2\pi/dr$, where $w = 200$ m and $dr = 0.20$ m are the surface length and the spatial sampling, respectively. The surface length is selected to be larger than the peak spectral wavelength $\lambda_p = 83.3$ m, and dr is such that $\lambda_{\min} = 2 \times dr$, the minimum wavelength on the free surface. In the following, we also assume that the LIDAR camera is located at $z_0 = 10$ m above the ocean mean water level, with its main axis of view pointing at a distance $d_0 = 50$ m ahead. The vertical aperture is $\theta_v = 13$ deg, and there are $n_{rv} = 64$ rays in the vertical plane.

Ocean surfaces are generated on the basis of the PM spectrum, as before, using a random phase method. We again use $N = 1024$ individual wavenumbers distributed over the selected range, with 512 positive and negative k values. The corresponding frequencies can be calculated using the linear dispersion relationship (1) assuming deep water waves, i.e., $\omega_n^2 = gk_n$.

Fig. 6 shows results of applying the interface reconstruction algorithms to simulated LIDAR data obtained from a unique snapshot of a 1-D CWM ocean surface. In the linear reconstruction algorithm results shown in Fig. 6(a) and (b), we use $N_k = 40$ or 400 wavenumbers, logarithmically spaced between 0.07 and 3.1 rad/m ($\lambda_{\max} = 90$ m and $\lambda_{\min} = 2$ m), respectively. Black dots represent the data set of simulated LIDAR observations. No additional noise, representing experimental errors, is included at this stage. As expected, the reconstruction is very accurate over the LIDAR footprint area, with only 40 wavenumbers, but the algorithm fails to reconstruct the surface outside this zone, where the inversion process is not constrained. The footprint area size is thus a major parameter and should be carefully defined as a function of the desired reconstructed wavelength interval.

Additionally, we see that, despite the paucity of data for the more distant waves resulting from shadowing effects (which is an expected characteristics of low incidence LIDAR data),

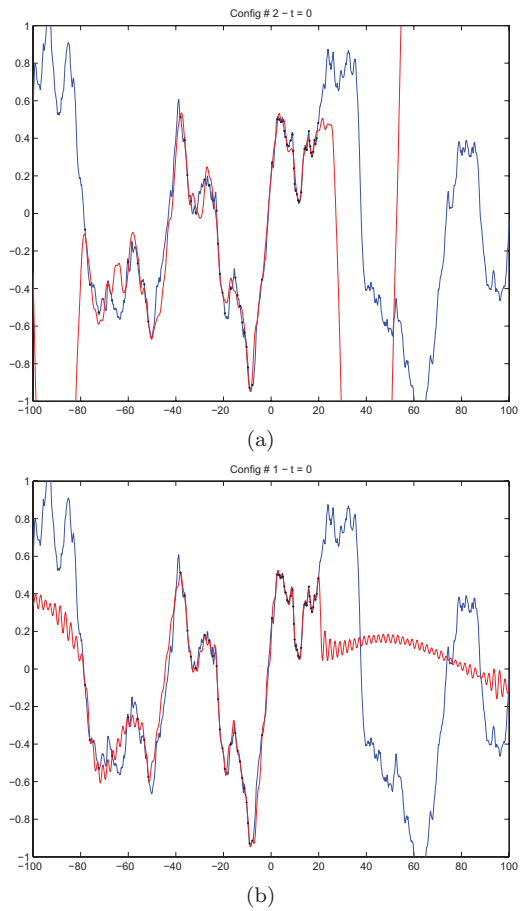


Fig. 6. Linear reconstruction of a 1-D CWM surface. Black dots: simulated LIDAR observations on the simulated surface (blue lines). Red lines: reconstructed surfaces with $N_k =$ (a) 40; (b) 400.

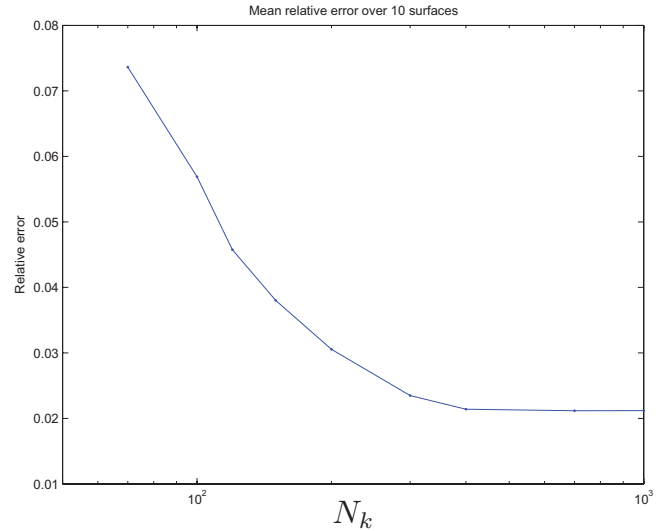


Fig. 7. Relative error of linear reconstruction of a CWM surface, versus the number of harmonics.

and particularly behind wave crests, the reconstructed surfaces capture well the salient features of the actual ocean surfaces, above the 2-m wavelength selected as the higher frequency cut-off in the algorithm. However, as indicated before, the surface sampling process is strongly nonuniform and the density of sampled points on the sea surface is strongly

decreasing with distance from the camera. Thus, the choice of the optimum number of reconstructed harmonics (N_k) is highly dependent on the LIDAR illuminating configuration.

The relative error of the reconstruction is plotted as a function of N_k in Fig. 7 for the specific illuminating configuration used above

$$\epsilon = \sqrt{\sum_{l=1}^{N_b} (\eta_r - \eta_s)^2 \times \left[\sum_{l=1}^{N_b} (\eta_s - \bar{\eta}_s)^2 \right]^{-1}} \quad (24)$$

where η_s , η_r and $\bar{\eta}_s$ are the simulated and reconstructed surfaces, respectively, taken at each sampled point, and the mean elevation of the simulated surface. On Fig. 7, each marked data point was obtained by averaging the relative error over ten test surfaces. A good compromise between accuracy and computational time is obtained around $N_k = 400$ harmonics, which corresponds to about ten times the order of magnitude of observations points. However, other simulations with higher wind speeds show that increasing N_k no longer improves reconstruction once the maximum wavelength becomes significantly larger than the camera's footprint size. This confirms that the camera configuration (e.g., aperture angle) must be adapted to wind conditions.

C. Reconstruction and Prediction Through Time Integration

At this point, our inversion scheme suffers that a data set obtained from a single snapshot of the surface at a given time does not provide enough information to discriminate between wave propagation directions (i.e., upwind or downwind in 1-D). Therefore, a time-dependent data set is required with the additional advantage of accessing some new points on the surface, which may have been hidden by a foreground wave crest at previous time steps.

As an example, we generated 1-D LIDAR data sets, using the previous camera configuration, over a simulated nonlinear CWM surface with parameters : PM spectrum; $U_{19.5} = 7$ m/s; surface length of 200 m; spatial step of 20 cm. We assumed that waves propagated in both positive and negative x directions in a dissymmetric manner with: 90% of the spectral energy associated with the wind direction (positive x) and 10% opposite to wind direction (negative x). Maximum and minimum wavelengths were, respectively, set to 45 m and 40 cm and the peak wave celerity to $c_p = 8$ m/s. The LIDAR frequency of acquisition rate was set to 2 Hz, and thus a 64-point 1-D data set would be obtained every 0.5 s. The footprint of the LIDAR camera's aperture is around 100 m, as shown on Fig. 5. With 200 reconstructed harmonics spread over positive and negative wavenumbers, five to seven iterations in CWM inversion algorithm are usually needed.

As remotely sensed waves are moving during time acquisition by the camera, it is no longer justified to define a relative error between simulated and reconstructed surfaces over the footprint area. Since the targeted application for this project is to derive the best estimate of the sea state in front of a (moving) vessel, in order to find the best way to steer it through a given sea state, we define a new zone where the sea state estimate is useful for the vessel's path prediction. In the example below, we decided that this "prediction zone" is spanning from around 20 m in front of the vessel (i.e.,

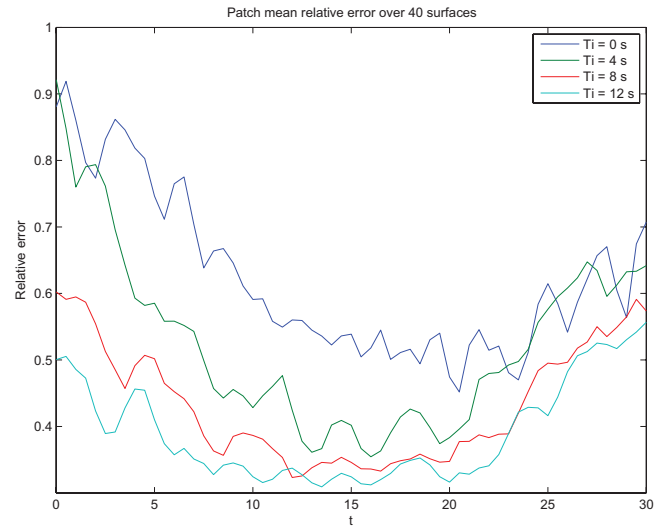


Fig. 8. Relative error versus forecasting time in the prediction zone. Acquisition frequency 2 Hz.

20 m in front of the camera) and the relative error of the reconstruction would thus be evaluated over this zone. Hence

$$\epsilon = \frac{1}{\sigma_\eta} \sqrt{\frac{1}{N_z} \sum_{l=1}^{N_z} ((\eta_r - \bar{\eta}_r^z) - (\eta_s - \bar{\eta}_s^z))^2} \quad (25)$$

where the simulated surface variance is defined as

$$\sigma_\eta^2 = \frac{1}{N_b} \sum_{l=1}^{N_b} (\eta_s - \bar{\eta}_s)^2 \quad (26)$$

where N_z is the number of simulated points in the "zone of prediction" and N_b is the total number of point of the simulated surface. $\bar{\eta}_r^z$ and $\bar{\eta}_s^z$ are the mean surface elevation of the reconstructed and the simulated surfaces, respectively, over the zone of prediction and $\bar{\eta}_s$ is the mean elevation of the whole simulated surface (usually zero). Such a definition implies that the error is not sensitive to wavelengths greater than the zone of prediction size. We recall here that the free surface variance is related to the significant wave height as, $H_s = 4\sigma_\eta$.

We tested four data sets, with different measuring times from 0 to 12 s (i.e., 1–25 surface snapshots with a 2-Hz data acquisition frequency), and computed the relative errors defined by (25), between the simulated and reconstructed surfaces. Fig. 8 shows the relative error over the "prediction zone" as a function of time. For instance, the red curve labeled $T_i = 8$ s means that data acquisition took place between $t = -8$ and $t = 0$ s. At $t = 0$ s, remotely sensed waves have not yet reached the prediction zone and hence the simulated and reconstructed surfaces are still significantly different. Around $t = 15$ s most sensed waves have reached the "prediction zone" and the relative error reaches a minimum before increasing again once waves have passed by the vessel. Errors plotted in Fig. 8 are averaged over 40 nonlinear CWM surfaces, to obtain smooth curves. Fig. 8 thus shows that the prediction accuracy cannot be as good as that of a mere inversion of a unique snapshot, and is dependent on the acquisition time. This is because the entire range of simulated wavelengths is not inverted and sensed wave are moving with

different velocities; hence this yields an unavoidable minimum error. An alternative error, defined for waves only belonging to the range of interest, could have been introduced, but it could not be used in practical tests. Nevertheless, Fig. 8 shows that a forecast is clearly possible and that Time-dependent data acquisition is highly desirable for improving sea surface prediction.

The error oscillations in Fig. 8 are due to the inability to estimate properly the propagation direction of waves with a frequency exactly equal to half the LIDAR frame rate. Indeed, such waves exactly travel half their wavelength between two illuminations of the surface. It is therefore impossible to evaluate their propagation direction. This phenomenon will be explained in more details in the 2-D case. A consequence of this limitation is that error oscillate at the same frequency (half the camera frame rate) and with an amplitude proportional to the corresponding wave amplitude.

In any case, the longer the measurement time, the larger the prediction time window and the smaller the error. More specifically, if one wishes to predict the sea state “ n ” seconds in the future, one needs to observe (i.e., sense) waves in the wavelength range of interest, which will reach the “prediction zone” in “ n ” seconds. A continuous real-time inversion will keep the relative error to the minimum level and is thus the best option. However, for vessel path prediction, sea state forecasting must be achieved for “prediction zones” located near the camera footprint area, rather than close to the vessel’s stern; one would expect even smaller errors in these zones. Note, in practical applications, the useful forecasting zones will also be dependent upon vessel speed. A complete study of the inversion algorithm performance as a function of all the parameters including vessel speed is left out for future work.

V. RECONSTRUCTION AND PREDICTION OF 2-D SURFACES

Forecasting 2-D ocean surfaces on the basis of reconstruction with LIDAR data is the main goal of this work. Here, we validate the 2-D algorithms assuming a slightly reduced wind speed of 5 m s^{-1} and generating the ocean surface between -70 and $+70$ m in the wind direction and between -36 and $+36$ m in the crosswind direction. This is a minimum configuration, which reduces the computational effort while still allowing us to correctly model the surface in terms of mean square elevation and peak wave length.

The LIDAR camera parameters are also selected as a minimum configuration: ($n_{rv} = n_{rh} = 64 \times 64$ rays (i.e., 4096 LIDAR rays) and frequency of data acquisition: 1 Hz (i.e., $\Delta t = 1$ s), which should represent an achievable hardware with current Flash LIDAR technology. For the purpose of illustration, the camera is located at $x_0 = 70$ m, $y_0 = 0$ m, and placed at $z_0 = 10$ m above mean sea level. The camera’s main axis of view is pointing at a distance $d_0 = 50$ m ahead, so that the main wind wave direction is toward the camera; the vertical aperture is $\theta_v = 13$ deg. and the horizontal aperture $\theta_h = 30$ deg. The LIDAR configuration and footprint surface are shown in Fig. 9. The red area closer to the camera position represents the “prediction zone,” over which we will compute the relative error of the forecasted surface in the following simulations.

We randomly generate 2-D nonlinear CWM surfaces on the basis of an EY directional energy density spectrum, with

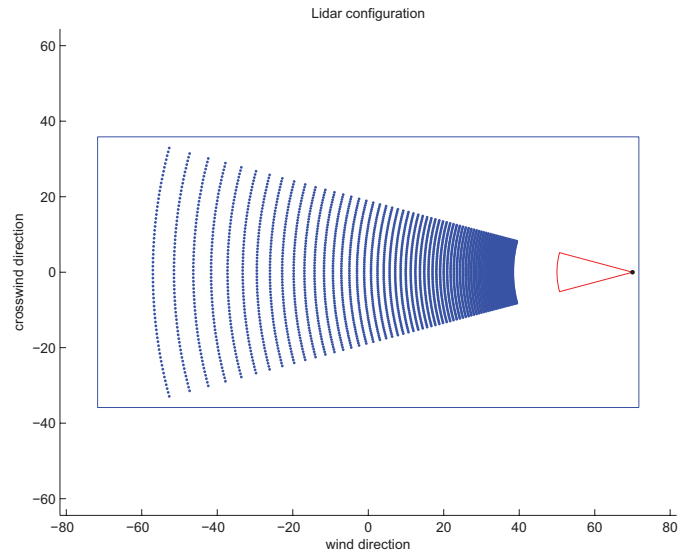


Fig. 9. Geometric configuration of the 2-D reconstruction problem using a Flash LIDAR camera located at $x_0 = 70$ m, $y_0 = 0$, and $z_0 = 10$ m (blue lines) simulated surface limits; (blue dots) LIDAR ray intersections with the horizontal plane; and (red area) “prediction zone.”

$U_{10} = 5 \text{ m s}^{-1}$ The peak spectral wave has a $\lambda_p = 23$ m wavelength or a phase speed $c_p = 6$ m/s, for a peak spectral period $T_p = 3.81$ s. The energy spectrum is truncated in both the along-wind and crosswind directions at $k_{\max} = k_e/2$, where $k_e = 2\pi/dr$ is Shannon’s wavenumber ($dr = 0.28$ m). The low cut-off of the spectrum is defined as $k_{\min} = 2\pi/L$, where L is the surface length in the considered direction. Fig. 10 shows a 145×70 m simulated surface, generated over 512×256 points with a 0.28 m spatial sampling. The surface is generated by fast Fourier transform with 512×256 harmonics. Wind blows in the positive x direction.

Fig. 10 also shows the simulated 2-D LIDAR data set at $t = 0$ s, yielding $L = 4096$ simulated observations, where the Flash LIDAR camera rays intersect the ocean surface. Based on preliminary results, we decided to distribute the reconstructed harmonics over a polar coordinate grid, rather than a Cartesian one. To reduce computational effort, we used only a small number $N_k = 71$ of wavenumber norms, which were selected as logarithmically spaced within the interval $[0.1, 3.1]$ rad/m ($\lambda \in [2, 63]$ m) and $N_\theta = 70$ azimuths, linearly spaced within the interval $[0, 2\pi]$. This leads to positive and negative wavenumbers for both the along- and across-wind directions. With these parameters, 4970 pairs of (a_n, b_n) coefficients are calculated in the LMS minimization performing the free surface reconstruction.

Fig. 11 shows the reconstructed linear surface at $t = 0$ s of Fig. 10. As in the 1-D case, the reconstructed free surface captures well the salient features of the simulated ocean surface. Fig. 12 compares vertical cross sections through both surfaces, along five azimuthal directions relative to wind direction (x), versus distance from camera. As expected, only the properly illuminated part of the simulated surface is correctly reconstructed. However, the relative error between the simulated and reconstructed surfaces in the “prediction zone,” based on a single snapshot exceeds acceptable values, as previously observed for 1-D cases.

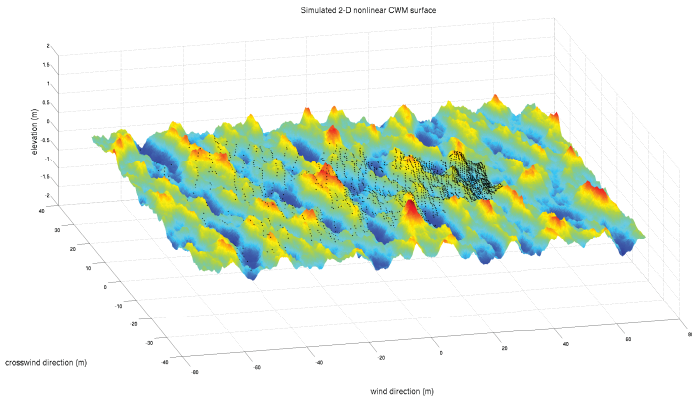


Fig. 10. Example of simulated 2-D nonlinear CWM ocean surface for a EY spectrum with $U_{10} = 5$ m/s blowing in positive x direction ($\lambda_p = 23$ m). Black dots mark Flash LIDAR camera rays intersections with the simulated ocean surface.

Hence, as in 1-D, we perform a 2-D reconstruction using a finite measurement/observation time T_i . As in 1-D, where spectral energy was arbitrarily spread over the upwind and downwind directions, we also introduce a modification of the directional wave energy spectrum, representing an upwind/downwind dissymmetry. Thus, in time-dependent simulations, we define the linear wave harmonic amplitudes as

$$A_n = \sqrt{2S(k_n, \Theta_n) \cos^2(\Theta_n/2) k_n \Delta k \Delta \Theta_n}. \quad (27)$$

The assumed directional wave energy distribution is shown in Fig. 13(a). Time evolution is carried out by marching forward in time both the simulated and reconstructed surfaces, and relative errors are calculated between both of these, as an average over 48 surfaces to obtain smooth curves. Fig. 14 shows relative errors over the “prediction zone” as a function of forecasting time, for various observation time T_i , with $T_i = n$ implying the camera acquires data between $t = -n$ and $t = 0$ s. Results correspond to a 1-Hz acquisition frequency. While relative errors vary with forecasting time qualitatively as in 1-D, they are larger than in 1-D. This can be explained first by the smaller number of harmonics used here and second by waves propagating from large azimuthal directions relative to the camera’s axis, which are not observed and hence cannot be reconstructed.

Fig. 13 shows the simulated and reconstructed wave amplitudes over the reconstructed wavenumbers for a few T_i values. As expected, up to some maximum forecasting time, the greater the measurement time and the smaller the reconstruction error, the better the wave energy distribution estimate (amplitude and directionality). However, even if the latter is good at large azimuths, the reconstructed waves in this wavenumber domain will probably not cross the prediction zone as they are merely moving across the observation zone and thus do not contribute to error reduction in the prediction zone. To achieve a better estimate of phases for waves crossing the prediction zone it would be necessary to use a larger azimuthal aperture of the camera (this could be easily simulated later).

The circle observed on Fig. 13(d) at wavenumber norm $k = 1$ is an artifact of having a regular camera sampling rate as already explained in Section IV-C. It corresponds to waves frequency ($f = 0.5$ Hz) with half the LIDAR camera frame

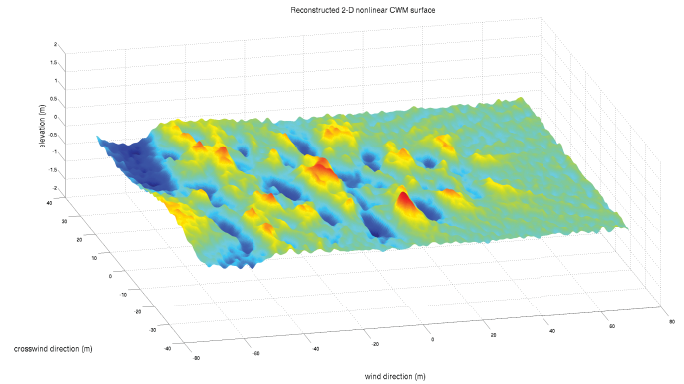


Fig. 11. Case of Fig. 10. Example of reconstructed 2-D nonlinear CWM surface; 4970 wavenumbers ($N_k = 71$ and $N_\theta = 70$) are used in the LMS inversion method.

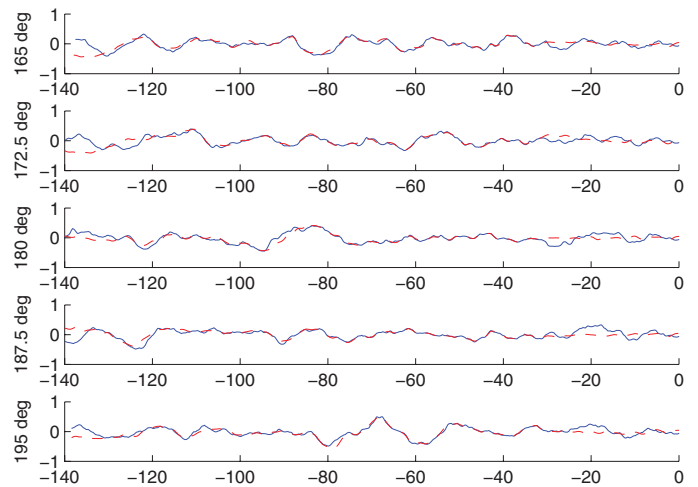


Fig. 12. Vertical cross-sections in simulated (solid - blue) and reconstructed (dashed - red) 2D nonlinear CWM surfaces for 5 azimuth angles. Abscissa values represent distance from the camera.

rate. For this particular wavelength, the wave direction cannot be determined and wave energy is equally spread over opposite wavenumbers. It results on an persisting 0.5-Hz oscillation error, which is clearly visible on Fig. 14.

We note that the best reconstruction time is obtained around $t = 5 - 10$ s, which corresponds to the time interval needed for reconstructed waves to reach the “prediction zone.” As shown in Fig. 14, the time window for an optimal reconstruction corresponding to the minimum error is dependent on the measurement time; other simulations also show that the minimum error decreases with the number of harmonics N_k used for the reconstruction. Hence, further improving the reconstruction of such sea states would require using longer measurement times and larger N_k values, and hence greater computational resources than used here for the purpose of method validation. Finally, in operational conditions, each inversion leading to interface reconstruction would likely benefit from results of the earlier ones; this would speed up calculations in the iterative GMRES solver and lead to better sea state estimates due to the inclusion of previous inversion results as initial condition.

A rigorous analysis of the predictable area in space-time for a directional wave field was proposed by Wu (2004), who

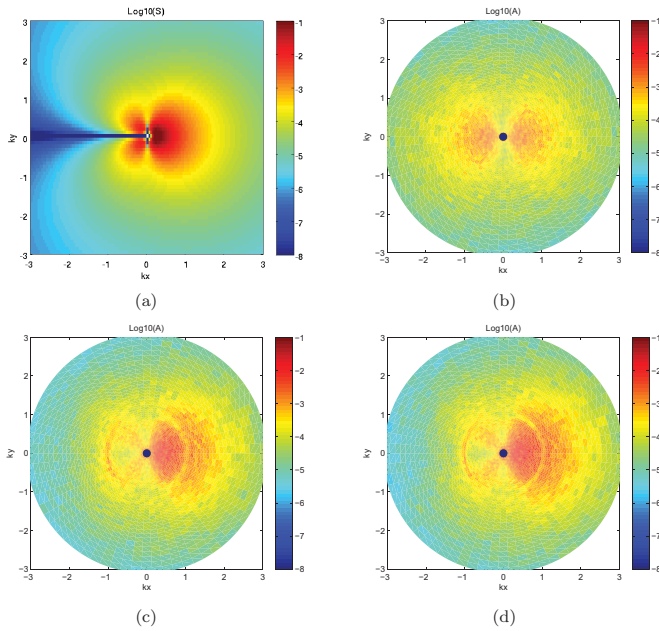


Fig. 13. Case of Fig. 12. Wave amplitude spectrum over the reconstructed wavenumber domain for various observation times T_i . Amplitudes are averaged over 48 surfaces. (a) Original waves amplitude. (b) Estimated waves amplitude $T_i = 0$ s. (c) Estimated waves amplitude $T_i = 4$ s. (d) Estimated waves amplitude $T_i = 8$ s.

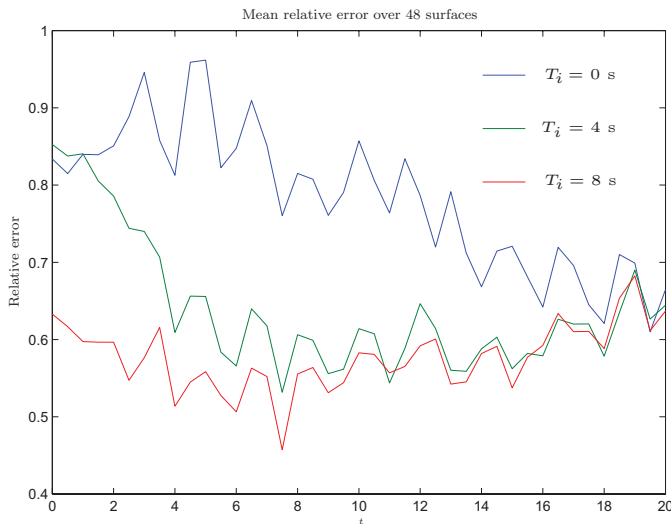


Fig. 14. Case of Fig. 12. Relative error between reconstructed and simulated nonlinear surfaces versus forecasting time over the “prediction zone,” for various observation times T_i . Acquisition frequency 1 Hz.

showed that, for a single probe (i.e., one spatial data point), the maximum prediction time is a function of the slowest and fastest wave components (in terms of group velocity, (2), i.e., c_g^{\min} and c_g^{\max} , respectively), that “cross” the measurement period T_i (8 s maximum here)

$$T_f = T_i \frac{c_g^{\max}}{c_g^{\max} - c_g^{\min}}. \quad (28)$$

The same work also showed how this prediction time can be increased by increasing the number of “wave probes.” In our test case, where wind speed is taken at 5 m/s, the inverted wavenumbers are $k_n = 0.1$ to 3.1 rad/m, the minimum and maximum group velocities of directional wave components

are, $c_g^{\min} = 0.85$, $c_g^{\max} = 4.77$ m/s; hence, the prediction time for one probe is limited to $T_f = 10$ s. Although we did not perform any detailed calculation for the large number of spatial “probes” that the intersecting LIDAR rays constitutes and the effect of the “prediction zone” maximum size and position relative to camera, we verified that $T_f = 10$ s is at or near the upper bound of what is acceptable for an accurate enough forecast in the selected spatial area. More work is clearly needed to better establish the relevant value of T_f as a function of all the problem parameters.

VI. CONCLUSION

Rather than finding the optimum configuration of the observing system our goal was to exemplify the possibilities of the linear and nonlinear sea surface inversion algorithm. To this end, a methodology of sea surface reconstruction and forecasting is applied to several 1-D and 2-D configurations, showing encouraging results in both cases. In this “proof of concept,” we thus concentrated on assessing the inversion algorithm efficiency and dependency on inversion parameters (e.g., N_k). Therefore, we on purpose limited the problems to particular cases, using a fixed camera location and specifications (i.e., vertical and horizontal angular aperture, aiming direction, ray numbers, acquisition frequency, etc.). To better optimize the problem parameters, the ideal “prediction zone” for assisting in vessel path steering should be defined first. Then, one would adjust the observation zone and observing LIDAR system orientation and parameters (e.g., aiming direction, aperture, data acquisition rate, etc.) as a function of the wind vector and the vessel speed. Indeed, observing waves just in front of the vessel may not be the best choice of camera orientation, since most of the waves that will cross the vessel path propagate along the wind direction. Additionally, because we used a fixed camera location in our simulations, the observed area remained the same; however, one could easily imagine that this area would change as the vessel is moving and hence would naturally provide more spatially decorrelated data at each acquisition time. This could lead to more accurate inversions, but would require a higher frequency of data acquisition. On the other hand, due to vessel motions, waves encountered during navigation will be different than those used in a static inversion; and waves traveling from the vessel sides become less important than waves propagating in the vessel direction. Thus, the camera azimuthal aperture could be chosen smaller than that in our study. We could also think of a uniform horizontal sampling of the surface (which implies a nonuniform angular sampling of the camera rays) to get a better estimation of the surface, assuming this is optically achievable.

As a first conclusion, one can state that the optimal LIDAR configuration will strongly depend upon the sea state (peak wave, wind speed, and direction) and vessel kinematics. However, we have established that a satisfactory inversion and prediction can easily be achieved using the current inversion algorithm. The method is also shown to be easily extendable to nonlinear surfaces and to yield good results for such cases, providing the measurement and prediction zones are commensurate.

We also showed in this paper that both 1-D and 2-D irregular ocean surfaces can be reconstructed as a *nowcast*, on the basis

of unevenly distributed simulated LIDAR observations. Both linear and choppy free surface generation and reconstruction algorithms were developed and validated. The best results were obtained when the LIDAR data set combines both spatial and temporal data, which is practically easy to achieve, considering the fairly high frequency of data acquisition anticipated for typical LIDAR cameras (i.e., 4–20 Hz). In the case of a 2-D linear reconstruction, using spatiotemporal data, we showed that a short-term *forecast* of the ocean surface can be accurately and efficiently (i.e., analytically) generated. Relative errors over the prediction zone can be as small as 15% of the significant wave height with a basic inversion algorithm parametrization (71 inverted wavenumbers for 70 different azimuths).

A larger data set (i.e., in terms of LIDAR rays/data points and frames) allows both for a better spectral description of the ocean surface (i.e., using a larger number of wave harmonics and providing a better coverage of the relevant frequency range), and a more accurate reconstruction (in terms of RMS difference with the actual surface), particularly in shadow areas behind wave crests. In such instances, the forecast is also expected to be improved and to stay reliable for a longer term forecast.

Linear or choppy reconstructions of the ocean surface were performed for both 1-D and 2-D cases. The use of the efficient iterative solver GMRES allows for a fast and accurate solution in few seconds on a standard laptop, with no particular optimization and classic interpreted software. Clearly, a multiple core or GPU implementation in a compiled language would reduce this time by one to two orders of magnitude. This optimization part of the numerical model will take place in future work.

Future work will also include a systematic assessment of the sensitivity of results to various numerical and model parameters as well as the effects of noise and measurement errors in simulated LIDAR data. Importantly, one should assess the effect of motion of the vessel (on which the LIDAR camera is mounted) on the spatiotemporal reconstruction of the ocean surface.

VII. ACKNOWLEDGMENT

F. Nouguier would like to thank Le Centre National de la Recherche Scientifique and Université du Sud-Toulon-Var (chaire mixte) for their support.

REFERENCES

- [1] F. Nouguier, C. A. Guérin, and B. Chapron, "Choppy wave model for nonlinear gravity waves," *J. Geophys. Res.—Ocean.*, vol. 114, no. C13, p. 09012, 2009.
- [2] J. T. Johnson, R. J. Burkholder, J. V. Toporkov, D. R. Lyzenga, and W. J. Plant, "A numerical study of the retrieval of sea surface height profiles from low grazing angle radar data," *IEEE Trans. Geosci. Remote Sens.*, vol. 47, no. 6, pp. 1641–1650, Jun. 2009.
- [3] H. Dankert and W. Rosenthal, "Ocean surface determination from X-band radar-image sequences," *J. Geophys. Res.*, vol. 109, no. C4, p. C04016, 2004.
- [4] J. C. Nieto Borge, G. R. Í. Rodríguez, K. Hessner, and P. I. González, "Inversion of marine radar images for surface wave analysis," *J. Atmos. Ocean. Technol.*, vol. 21, no. 8, pp. 1291–1300, 2004.
- [5] C. S. Chae and J. T. Johnson, "A study of interferometric phase statistics and accuracy for sea surface height retrievals from numerically simulated low-grazing-angle backscatter data," *IEEE Trans. Geosci. Remote Sens.*, vol. 49, no. 11, pp. 4580–4587, Nov. 2011.

- [6] M. R. Belmont, R. Horwood, W. F. Thurley, and J. Baker, "A shallow angle wave profiling lidar," *J. Atmos. Ocean. Tech.*, vol. 24, pp. 1150–1156, Aug. 2006.
- [7] G. Wu, "Direct simulation and deterministic prediction of large-scale nonlinear ocean wave-field," Ph.D. dissertation, Dept. Ocean Eng., Massachusetts Inst. Technol., Cambridge, MA, USA, 2004.
- [8] E. Blondel, "Reconstruction et prévision déterministe de houle à partir de données mesurées," Ph.D. dissertation, Dept. French Grande école Eng., Univ. Ecole Centrale de Nantes, France, 2009.
- [9] E. Blondel, F. Bonnefoy, and P. Ferrant, "Deterministic non-linear wave prediction using probe data," *Ocean. Eng.*, vol. 37, no. 10, pp. 913–926, 2010.
- [10] R. G. Dean and R. A. Dalrymple, *Water Wave Mechanics for Engineers and Scientists*. Upper Saddle River, NJ, USA: Prentice-Hall, 1984.
- [11] T. Elfouhaily, B. Chapron, K. Katsaros, and D. Vandemark, "A unified directional spectrum for long and short wind-driven waves," *J. Geophys. Res.*, vol. 102, no. C7, pp. 15781-1–15781-15, 1997.



Frédéric Nouguier received the "Agrégation" and M.S. degrees in applied physics from the Ecole Normale Supérieure de Cachan, Paris, France, in 2005 and 2006, respectively, the M.S. degree in physical methods for remote sensing from the University of Paris-Diderot, Paris, in 2006, and the Ph.D. degree in physics from the University of Marseille, Bouches-du-Rhône, France, in 2009.

He was a Post-Doctoral Fellow with the French Research Institute for Exploitation of the Sea (IFREMER), Brest, France, from 2009 to 2010. He was

working on synergical studies of optical and synthetic aperture radar sensor products in mesoscale and submesoscale ocean dynamics interpretation at IFREMER, as a European Space Agency Post-Doctoral Fellow in 2011. He is currently an Associate Professor with the Mediterranean Institute of Oceanography, Toulon, France.



Stéphan T. Grilli received the M.S. and Ph.D. degrees from the University of Liège, Liège, Belgium.

He moved to the USA in 1987. He spent three years as a member of research faculty with the University of Delaware, Newark, DE, USA, before he joined the faculty of the University of Rhode Island, Narragansett, in 1991, where he is currently a Distinguished Engineering Professor of Ocean Engineering and a Professor of oceanography. He studies ocean waves, tsunamis, and related fluid mechanics

and marine hydrodynamics problems. He also studies waves induced by underwater landslides. His current research interests include the numerical modeling of complex nonlinear wave flows, such as wave breaking, extreme wave effects on ocean structures, and wave-induced sediment motion in coastal regions.



Charles-Antoine Guérin received the B.Eng. degree from the Ecole Nationale Supérieure de l'Aéronautique et de l'Espace, Toulouse, France, in 1994, and the Ph.D. degree in theoretical physics from the University of Aix-Marseille I, Marseille, France, in 1998.

He is currently a Professor and Researcher with the Geosciences and Remote Sensing Department, Laboratoire de Sondages Electromagnétiques de l'Environnement Terrestre, Centre National de la Recherche Scientifique/Université du Sud-Toulon-Var, La Garde Cedex, France. He is specializing in electromagnetic wave theory and its application to ocean remote sensing.